Mesothelin-targeted MRI for assessing migration, invasion, and prognosis in malignant pleural mesothelioma

Yilong Huang[1†], Shasha Shen[1†], Jie Xiao[2], Cici Luo[3], Jiyao Ma[1], Xin Huang[3], Tianfu Qi[1], Chao Gao[1], Guiyun Li[4], Fan Li[5], Bo He[1], Bingdi Chen[3*] and Dan Han[1*]

[†]Yilong Huang and Shasha Shen contributed equally to this work.

*Correspondence:
inanochen@tongji.edu.cn;
handan6@kmmu.edu.cn

[1] Department of Medical Imaging, First Affiliated Hospital of Kunming Medical University, No. 295 Xichang Road, Kunming 650032, Yunnan, China
[2] Department of Pathology, Huangshi Central Hospital, Affiliated Hospital of Hubei Polytechnic University, Hubei, China
[3] The Institute for Biomedical Engineering and Nano Science, Tongji University School of Medicine, No. 67, Chifeng Road, Yangpu District, Shanghai 200092, China
[4] Department of Pathology, First Affiliated Hospital of Kunming Medical University, Yunnan, China
[5] Department of Pathology and Pathophysiology, School of Basic Medical Sciences, Kunming Medical University, Yunnan, China

Abstract

Background: Mesothelin (MSLN) has been implicated in cancer migration, invasion, and prognosis, making it a potential tumor marker. However, the precise role of MSLN in the migration and invasion of malignant pleural mesothelioma (MPM) remains elusive, and effective noninvasive methods for assessing MSLN status are currently lacking. In this study, we focused on MSLN expression and elucidated the underlying mechanisms by which MSLN regulates migration and invasion in MPM. Building upon this knowledge, we developed an MRI nanoprobe that targets MSLN to assess its status in vitro and in vivo by comparing T2 signal intensity and T2 values on magnetic resonance imaging examinations. This nanoprobe combines the anatomical information obtained from MRI with biological information obtained from MSLN for comprehensive evaluation of MPM.

Results: Notably, we observed that MSLN expression in the epithelial type of MPM was higher and increased continuously with tumor growth than that in other types. In addition, MSLN upregulation promoted N-cadherin, matrix metalloproteinase-7, and MMP9 expression and resulted in higher migration/invasion ability and shorter survival. We synthesized MSLN-targeted nanoprobes ($Fe_3O_4@SiO_2$-PEG-MSLN, FSPM) to assess MSLN expression by comparing the T2 signal intensity and T2 value of different cell lines and mice after 14, 28, and 42 days of modeling. Remarkably, MSLN-targeted nanoprobes demonstrated excellent targeting capabilities. In vitro studies revealed a pronounced reduction in T2 signal intensity and T2 values of the epithelial type as the probe concentration increased. In addition, in vivo experiments demonstrated a gradual decline in these parameters over time, particularly in the epithelial type as compared to the biphasic type, corresponding to the dynamic expression patterns of MSLN during different growth stages.

Conclusion: Our comprehensive research succeeded in confirming the regulatory mechanisms by which MSLN influences migration and invasion. Moreover, we introduced a promising method for monitoring MSLN expression that may help in facilitating the early detection, histological subtype identification, and assessment of migration, invasion, and prognosis in MPM.

Background

Malignant pleural mesothelioma (MPM) is an extremely aggressive rare malignancy with a poor prognosis. Although progress has been made in the early detection and treatment of MPM, 5-year survival rates have remained at < 5% for several decades (Lo Russo et al. 2018). Exposure to asbestos increases the chances of developing MPM (Craighead and Mossman 1982). Therefore, MPM incidence is related asbestos distribution, which is more prevalent in North America, Western Australia, Norway, and Dayao in China (Mensi et al. 2015; Luo et al. 2003). Although asbestos is banned, MPM incidence continues to rise due to its long incubation period of 30–40 years (Liu et al. 2017). MPM's poor prognosis is related to the lack of not only effective treatment options, but also early detection, staging, and prognosis prediction methods. Therefore, a noninvasive technique needs to be urgently developed to detect MPM, identify its histological subtypes, and predict patient prognosis.

Recently, conventional imaging modalities, such as computed tomography (CT), magnetic resonance imaging (MRI), and positron emission tomography (PET), have reportedly played an integral role in MPM's diagnosis, staging, and prognosis (Nickell et al. 2014; Zhang et al. 2023). However, benign and malignant pleural thickening are very similar, and high uptake of fluorodeoxyglucose (FDG) also occurs in inflammatory pleural diseases (Sinha et al. 2020), which limits conventional imaging usage. Targeted imaging may compensate for the lack of conventional imaging, provided specific markers are found. To date, several serum and tissue biomarkers have been employed for early detection and diagnosis (Vigneswaran et al. 2017; Wang et al. 2021). Interestingly, the Food and Drug Administration (FDA)-approved MSLN is highly aberrantly expressed in MPM, pancreatic, ovarian, and lung cancers, whereas benign lesions and normal tissues have lower expression (Zhang et al. 2014). Besides, Protease hydrolyzes cell surface MSLN to produce soluble mesothelin-related peptide (SMRP), which can be detected using enzyme-linked immunosorbent assay (ELISA) kits (Katz et al. 2021). Hollevoet et al. showed that > 80% of MPM cells express MSLN; expression varies among histological subtypes, with high expression of MSLN in the epithelial type and low expression in the biphasic and sarcomatous types of MPM (Hollevoet et al. 2012). Consequently, MSLN can also be used to differentiate between the histological subtypes of MPM (Pastan and Hassan 2014). Thus, MSLN can help in treatment selection and prognostic prediction.

In addition, tumor migration and invasion into the lungs and mediastinum are the main causes of MPM-related death. MPM cell migration and invasion capacity are related to prognosis and survival (An et al. 2010); analyzing MPM migration and invasion might increase our understanding of the prognosis. MSLN is reportedly involved in cancer cell migration and invasion (Shen et al. 2022; Shimizu et al. 2012). Unfortunately, MSLN's biological role in MPM remains unclear. MSLN reportedly promotes cell invasion in ovarian cancer by inducing matrix metallopeptidase-7 (MMP-7) expression (Chang et al. 2012). In addition, MSLN binds carbohydrate antigen 125 (CA125)/mucin 16 (MUC16) and activates MMP-7 to promote pancreatic cancer cell migration and invasion (Chen et al. 2013).

Thus, MSLN may strongly influence motility and invasion in MPM; however, the exact regulatory mechanism is still unclear. Furthermore, rare, good, and noninvasive methods are available for assessing MSLN status. Molecular imaging with specific markers can be used in vitro and in vivo with noninvasive imaging to target specific cells or tissues and capture molecular information from living cells (Rowe and Pomper 2022; Li et al. 2022). The MSLN monoclonal antibody of clone 11–25 was successfully labeled with ^{64}Cu (^{64}Cu-DOTA-11–25 mAb), which was used as an in vivo PET imaging probe to detect MSLN expression in pancreatic cancer. The study showed that compared to MSLN-negative tumors, ^{64}Cu-DOTA-11–25 significantly accumulated in tumors expressing MSLN (Kobayashi et al. 2015). In addition, two types of anti-MSLN single-domain antibodies labeled with ^{99m}Tc (^{99m}Tc-A1, ^{99m}Tc-C6) were studied both in vitro and in vivo. The results showed that 99mTc-A1 is a promising tracer for detecting tumors expressing mesothelin, which will help in detecting metastatic lesions and thus determining the prognosis (Montemagno et al. 2018). Although radiolabeled anti-MSLN nanobodies have been described for noninvasive imaging of MSLN-positive tumors. The MRI nanoprobes are extremely valuable in assessing the invasiveness and predicting the prognosis of MSLN-positive tumors due to their nonradiation, high spatial resolution, and unique multi-functional multi-parametric imaging, providing more valuable functional parameters.

Given the nanomaterials used to integrate molecular biomarkers are important for developing molecular imaging-specific contrast agents (Hao et al. 2022). Superparamagnetic iron oxide nanoparticles (SPIONs) have been extensively applied due to their biocompatibility and hypotoxicity in biomedicine (Żuk et al. 2021). They are used clinically as negative contrast agents for MRI and can reduce the T2-weighted imaging (T2WI) signal by diminishing the lateral relaxation time (Jarockyte et al. 2016). Moreover, the surface of SPIONs can bind various functional components and biomolecular markers. Gao et al. used SPIONs to bind folic acid and active penetrating peptides, which can improve lung cancer targeting by MRI and enhance reactive oxygen radical production in lung cancer cells; thus, promoting apoptosis (Gao et al. 2018). SPIONs nanomaterials can differentiate between benign and malignant tumors, display tumor lesions, and help evaluate the efficacy of therapeutic interventions (Bulte 2019; Ghosh et al. 2013) as demonstrated by Prantner et al. and Liu et al. MRI-targeted agents formed by MSLN antibody-conjugated SPIONs can diagnose pancreatic and ovarian cancers with higher sensitivity and specificity than classical gadolinium agents (Prantner et al. 2018; Liu et al. 2016). However, few noninvasive methods combine the anatomical information obtained from CT and MRI examinations with the biological information from antibodies to evaluate MPM prognosis.

Here, we confirmed the underlying MSLN mechanisms in MPM migration and invasion. Subsequently, based on the MSLN biological function, SPION nanoprobes modified with MSLN (designated $Fe_3O_4@SiO_2$-PEG-MSLN, FSPM) were synthesized to evaluate MSLN status using T2WI and T2 mapping MRI imaging.

Materials and methods

Cell lines and animals

The normal human pleural mesothelial cells (MeT-5A), and MPM cell lines, including epithelial (NCI-H226) and biphasic (MSTO-211H) were all from the Meisen Chinese Tissue Culture Collections (Zhejiang, China). NCI-H2452 of MPM epithelial cell line

and human lung adenocarcinoma A549 were purchased from the Procell Life Science & Technology Co, Ltd. (Wuhan, China). A549 and MPM cells were cultured in RPMI 1640 medium supplemented with 10% fetal bovine serum (FBS), 100 units of penicillin per mL (U/mL), and 100 mg of streptomycin per mL (mg/mL). MeT-5A cells were maintained in a medium containing 10% FBS, 100 U/mL penicillin, and 100 mg/mL streptomycin (M199). Each cell type was maintained at 37 °C, 95% humidity, and 5% carbon dioxide.

We purchased female nude mice ($n = 110$, 16–22 g, aged 4–6 weeks old) from Kunming Medical University (Kunming, China), and kept them at 20–22 °C under pathogen-free conditions. After successful tumor transplantation, 93 mice were used in the experiment.

Mesothelin expression of MPM

Immunoblotting

Total cell lysates and cytosolic and nuclear extracts for western blotting analysis were prepared as described elsewhere (Xie et al. 2012). Cells were lysed in a modified radioimmunoprecipitation assay solution containing a protease/phosphatase inhibitor cocktail (Beyotime, China) after three washes in ice-cold phosphate-buffered saline (PBS). Bicinchoninic acid test kits were used to evaluate protein concentration (Beyotime, China). The samples were heated to 95 °C for 5 min in a 5 sodium dodecyl sulfate (SDS)-sample buffer solution. Equivalent protein quantities (40 µg) were fractionated using 12% SDS–polyacrylamide gel electrophoresis before being transferred to polyvinylidene fluoride layers. After overnight incubation at 4 °C with the essential antibodies, the films were blocked with a 5% nonfat powdered drain in Tris-buffered saline Tween (TBST) for 1 h. The membranes were subsequently rinsed three times with TBST, incubated with peroxidase-conjugated goat anti-rabbit auxiliary antibodies, and then washed three times with TBST. The antigen–antibody complexes were recognized using an improved chemiluminescence reagent (Beyotime, China). The anti-MSLN antibody (clone EPR4509, ab133489, USA) served as the primary antibody, and actin (45 kDa, cytosolic protein) was used as an internal reference. The expression levels were quantified using the ImageJ software (National Institutes of Health, USA).

RNA separation and quantitative real-time polymerase chain reaction (PCR)

Gross RNA was extracted from A549, MeT-5A, H2452, H226, and MSTO-211H cells using TRIzol reagent (Promega, USA) according to the manufacturer's instructions. According to the manufacturer's guidelines, 1 µg of RNA was used to synthesize complementary DNA (cDNA, Thermo Fisher, USA). The primers mentioned in Additional file 1: Table S1 were used to quantify the mRNA, and the PCR settings which included a 10-min denaturation step at 95 °C, 15-s cycles at that temperature for 40 cycles, 1 min of annealing at 60 °C, and a final extension step of 30 s at 72 °C. MSLN mRNA expression was quantified and adjusted to glyceraldehyde-3-phosphate dehydrogenase (GAPDH) mRNA expression. The results were analyzed using the $2^{-\Delta\Delta CT}$ method.

Staining with immunohistochemistry (IHC)

Tissue slices (20 µm) were fixed in formalin, paraffin-embedded, dewaxed in xylene, hydrated, rehydrated with graded ethanol (70–100%), inhibited for endogenous

peroxidation by 0.3% hydrogen peroxide, and microwaved in citrate buffer to remove antigens for 10 min (pH 6.0). After overnight incubation at 4 °C with MSLN essential antibodies (MSLN counteracting agent dilution ratio, 1:100), immunostaining was performed for 1 h at room temperature using the optimal amount of horseradish peroxidase (HRP)-conjugated auxiliary antibodies with DAB as a chromogen. After counterstaining the sections with hematoxylin, the slices were photographed under a light microscope. Five microscopic fields of each slice were further analyzed using ImageJ software.

Serum SMRP measurement

Serum samples were collected from the peripheral blood of tumor-bearing nude mice to measure SMRP and frozen at − 80 °C until evaluation. Commercial ELISA kits (Meso-mark, Fujirebio Diagnostics, Inc.) were used to measure the SMRP levels (Cristaudo et al. 2011), conforming with the specifications provided by the manufacturer. Briefly, standards, controls, and serum samples diluted 1:101 were prepared, dispensed into 96-well microplates pre-coated with the 4H3 antibody, and incubated for 1 h at room temperature. The wells were washed and incubated with the OV569-HRP antibody for 1 h. After washing again, trimethylborate substrate was added for 15 min and a reaction termination solution was added to terminate the reaction. The optical density (OD) was measured at 450 nm using a spectrophotometer (GVD Reader, NT Laboratory, Italy), and the SMRP content in the sample was calculated based on the OD values of the standard and sample.

Overexpression of MSLN

Lentivirus-MSLN mimics were obtained from GenePharma Co. Ltd. (Shanghai, China). We obtained the optimal concentration of 1.0 μg/mL by plotting a kill curve using different concentrations of puromycin (0, 0.1, 0.2, 0.4, 0.6, 0.8, 1.0, 1.2, 1.5, 2, 0, 2.5, and 3.0 μg/mL), and H226 cell screening showed enhanced green fluorescent protein expression in nearly all surviving cells. There were 1×10^5 H226 cells in every 1 mL of the infected liquid. The lentivirus was introduced using a multiplicity of infection established in a preliminary study. Transfection was performed for 24 h, and the medium was replaced with 10% FBS. At 72 h post-infection, infection efficacy was assessed using a fluorescent inverted microscope (Zeiss, Germany). Cells successfully transfected with lentivirus showed higher MSLN expression and formed the experimental group (LV-MSLN). The control group was infected with the lentiviral vector (LV-NC), whereas the negative control group received no treatment (NC).

Scratch test

A scratch assay was performed to examine cell migration. MeT-5A, H2452, H226, MSTO-211H, NC, LV-NC, and LV-MSLN cells were grown to confluence in six-well plates at a density of 6×10^5 cells/well. Using a pipette tip with a capacity of 200 μL, we scraped the monolayer and washed away the cellular debris with PBS. After incubation, the cells were observed under an inverted microscope at 0, 6, 12, 24, and 36 h. The cell migration rate = (0 h scratch width − post culture scratch width)/0 h scratch width × 100%. Experiments were repeated three times to ensure accuracy.

Cell migration and invasion assays

For the cell migration test, 24-well plates covered with a polycarbonate membrane (pore size: 8 m) were used. For the cell invasion tests, the membranes were pre-coated with Matrigel (BD Biosciences, Franklin Lakes. NJ, USA). Cells were seeded at a density of 3×10^5 cells/well (migration) or 5×10^5 cells/well (invasion) in the upper chamber compartment using serum-free culture. Subsequently, the lower chamber was refilled with complete media (including 15% FBS), and the cells were incubated for a full day. Cells neither moving nor invaded in the upper chamber were removed by cotton buds. Cells that invaded or migrated beneath the film were preserved in methanol, stained with 0.1% crystal violet, observed under the microscope, and the quantification of crystal violet staining was achieved by measuring the OD values at 570 nm (OD_{570nm}).

Survival and growth analysis of nude mice bearing tumors

Tumor nodules formed at the injection site in nude mice 5 days after the tumor cells were subcutaneously injected. Subsequently, the size of the tumor was recorded once every 3 days. Using calipers, the greatest axial (*a*) and lateral (*b*) tumor diameters were measured and substituted into the formula V_{tumor} (mm^3) $= ab^2/2$ to obtain a growth curve for the tumor. It records not only the time of survival, but also the time of natural death.

Synthesis of the Fe$_3$O$_4$@SiO$_2$-PEG-MSLN (FSPM) nanoprobe
Materials

Aladdin Reagent Company (Shanghai, China) was the supplier for all initial reagents, including sodium acetate, ferric chloride hexahydrate ($FeCl_3 \cdot 6H_2O$), ethylene glycol, ammonium hydroxide, tetraethylorthosilicate, (3-aminopropyl) triethoxysilane, methanol, polyethylene glycol (PEG) diacid solution (molecular weight: 6000), and 1-ethyl-(3-dimethylaminopropyl) carbodiimide hydrochloride (EDC-HCl). Saiguo Biotech Co., Ltd. (Guangzhou, China) supplied the Cell Counting Kit-8 (CCK-8). Deionized (DI) water (18.2 Mcm) was used in all the studies. All the other compounds used in this investigation were of sufficient purity for analytical use and did not require further purification.

Fe$_3$O$_4$ nanoparticles preparation

Nanoparticles of Fe_3O_4 were synthesized via hydrothermal reactions (Uribe Madrid et al. 2015). Ethylene glycol (30 mL), sodium acetate (2.56 g), and $FeCl_3 \cdot 6H_2O$ (0.86 g) were mixed in a round-bottomed flask. The solution was thoroughly mixed via magnetic stirring and then put into an autoclave for 8 h at 200 °C. The obtained products (Fe_3O_4 nanoparticles) were collected by washing thrice with ethanol and water. Finally, the products were dispersed in DI water.

Preparation of Fe$_3$O$_4$@SiO$_2$-NH$_2$

To prepare Fe_3O_4@SiO$_2$-NH$_2$ (Uribe Madrid et al. 2015), 5 mL of Fe_3O_4 (50 mg/mL) was initially dispersed in 0.1 M HCl with ultrasonic treatment for 15 min. Then, we combined the treated Fe_3O_4 with ethanol and water (v/v $= 70/30$) and used ammonium hydroxide to increase the pH to 9.5. After that, 80 μL of tetraethylorthosilicate was

added, and the mixture was stirred for 24 h to obtain $Fe_3O_4@SiO_2$. To graft the amino group (Xing et al. 2012), 50 mL of (3-aminopropyl) triethoxysilane was added, stirred for 4 h, and precipitated with methanol. The precipitate was centrifuged and rinsed thrice with ethanol before being dispersed in DI water.

Preparation of FSPM

The aminosilane-coated Fe_3O_4 particles were blended in a 1:2 ratio with a COOH-PEG-COOH diacid solution (molecular weight: 6,000), followed by the addition of EDC-HCl (5 mg). The reaction mixture was stirred continuously overnight. After centrifugation and washing thrice, the resulting mixture ($Fe_3O_4@SiO_2$-PEG, FSP) was collected and redispersed in borate buffer (50 mM; pH 8.2) containing EDC−HCl, then coupled to the anti-MSLN antibody with molar ratio of 1:100 in PBS. After magnetic separation, the final polymer (FSPM) was dispersed in PBS.

Characterization

For FSPM nanoparticle (NP) morphological examination, a transmission electron microscope TEM (JEM 1200EX instrument, JOEL, Tokyo, Japan) was used. FSPM chemical components were identified using X-ray photoelectron spectroscopy (XPS), and nanoprobe iron ion (Fe^{3+}) concentration was measured using an inductively coupled plasma (ICP) emission spectrometer. PBS was diluted based on experimental requirements. Nanoprobe relaxation times ($T2$ transverse and $T1$ longitudinal) were measured at 37 ℃ through an MRI analyzer (Achieva 3.0 T Tx, Philips Healthcare, Best, Netherlands). Relaxivity rates $R_1(1/T1)$ and $R_2(1/T2)$ were calculated as slope from a plot of the $1/T1$ and $1/T2$ relaxation time (s^{-1}) vs Fe^{3+} concentration (mM). The biological stability of FSPM was studied by diluting it in saline and FBS at concentrations of 0, 20, 40, 60, 80, and 160 μg/mL, and then shaked in a thermostatic incubator at 37 ℃, After 0, 12, and 24 h, the samples were observed for any aggregation phenomenon (Additional file 1: Fig. S2).

Cell viability

FSPM nanoprobe cytotoxicity in H226 and A549 cells was assessed using a Cell Counting Kit-8 (CCK-8) assay. Initially, 5,000 cells are seeded into each well of a 96-well plate and grown at 37 ℃, 5% CO_2 incubator. The wells were then filled with with 100μL of the FSPM nanoprobe suspension at concentrations of 0, 25, 50, 100, and 200 μg/mL and incubated for 24 h. Untreated cells were used as controls. Next, each well was incubated with 10 μL of CCK solvent for 2 h. Finally, the absorbance was measured at 450 nm using a microtiter plate reader (PowerWave XS; Bio-Tek, Winooski, VT, USA). Each experiment was performed in triplicate.

Prussian staining

Cellular uptake was assessed using Prussian blue staining. Firstly, 24-well plates were used to cultivate H226 and A549 cells for 24 h in a complete medium. Further, 30 μL of the targeted MSLN probes (FSPM, 40 μg/mL)) and nontargeted ($Fe_3O_4@SiO_2$-PEG, FSP, 40 μg/mL) probes were poured into the wells and hatched for 1 h. After incubation, the medium was removed, and cells were rinsed three times with PBS. Following fixation for

10 min in 4% paraformaldehyde, the cells were stained with Prussian blue. After 30 min, the cells were incubated and rinsed with DI water. The cells were then stained with Prussian solution for 60 s and washed with DI water. After drying, the cells were observed under an inverted microscope for the presence of blue particles. Then, We used Image J to quantify the area of Prussian-stained cells.

In vivo distribution of Fe

Initially, 100 μL of FSPM and FSP at 800 mg/L was injected into two groups of nude mice bearing H226 cell tumors. Then, 2.5 h after injection (Liu et al. 2016), the mice were euthanized, and their heart, lungs, liver, spleen, kidneys, and tumor tissues were collected. Finally, the concentration of Fe^{3+} in the organs and tumors was measured using the ICP method described above.

Ex vivo analyses

Following the injection of saline and FSPM, the main organs of the nude mice (head, heart, liver, spleen, lung, and kidney) were collected, fixed in 4% formaldehyde for 0.5 h, dehydrated, paraffin-embedded, and stained with hematoxylin and eosin (H&E). Organs from both groups were compared using a microscope to check for abnormal alterations.

In vitro MRI imaging

To test the tumor cell-targeting ability of the FSPM nanoprobe, the probe was incubated with MeT-5A, MPM cells (H2452, H226, and MSTO-211H) and A549 cells and then examined using Achieva 3.0 T clinical MRI. Further, 2.5×10^5 cells/well were seeded in 12-well plates and treated with 0, 1, 10, 20, 40, or 60 μg/mL FSPM for 2 h. The cells were then resuspended in 200 μL of 0.5% low-melting-point agarose, rinsed with PBS, trypsinized, and centrifuged. Finally, T2WI and T2 mapping were performed on each sample. T2WI signal intensity and T2 values were obtained. The parameters used for scanning are listed in Additional file 1: Table S2.

In vivo MRI imaging

To evaluate whether the FSPM nanoprobes can target tumors in vivo, a real-time in vivo MRI imaging system was used to study the biodistribution of NPs at different time points in a xenograft model. In the present study, subcutaneously transplanted tumor models were developed using H226, MSTO-211H, and A549 cells. When the tumor size reached approximately 150 mm³, mice with tumors were randomly divided into three groups ($n = 27$ per group). On days 14, 28, and 42, the mice were intravenously injected with 100uL saline, FSP, or FSPM solution (The concentration of both FSP and FSPM was 0.8 mg/mL), respectively ($n = 3$ mice per group) through the tail vein. For each mouse, T2WI and T2 mapping were performed at 0, 0.5, 1.5, 2.5, and 3.5 h after injection, and T2WI signal intensity and T2 values were scored.

Statistical analysis

Student's *t* tests were used to ascertain the differences between groups. One-way analysis of variance was used to examine differences among groups, followed by Tukey's post hoc analysis. All statistical analyses were performed using SPSS (version 22.0;

IBM Corp., Armonk, NY, USA). Between group differences were deemed significant (*) at $p < 0.05$ and extremely significant (**) at $p < 0.01$.

Results

Differential expression of MSLN in MPM subtypes

To determine the role of MSLN in MPM, we first evaluated MSLN expression levels in different histological subtypes of MPM cell lines (NCI-H226, NCI-H2452, and MSTO-211H) by western blotting and RT-PCR assays. Compared with the human lung adenocarcinoma cell line (A549) and the human normal mesothelial cell line (MeT-5A), MPM cell lines showed higher expression of MSLN (Fig. 1A and B). In addition, MSLN expression was higher in H226 cells than in H2452 or MSTO-211H cells. We further evaluated the level of MSLN protein in the tumor tissues of tumor-bearing nude mice at 14, 28, and 42 days after molding, using western blot analysis and IHC staining. H226 tumor tissues had higher protein levels of MSLN than the MSTO-211H and A549 groups. The MSTO-211H and H226 groups showed continuous increases in MSLN levels as the tumors grew, with H226 cells exhibiting higher levels than MSTO-211H cells during the same period (Fig. 1C and D). This was further validated by ELISA to detect the serum SMRP levels of A549, MSTO-211H, and
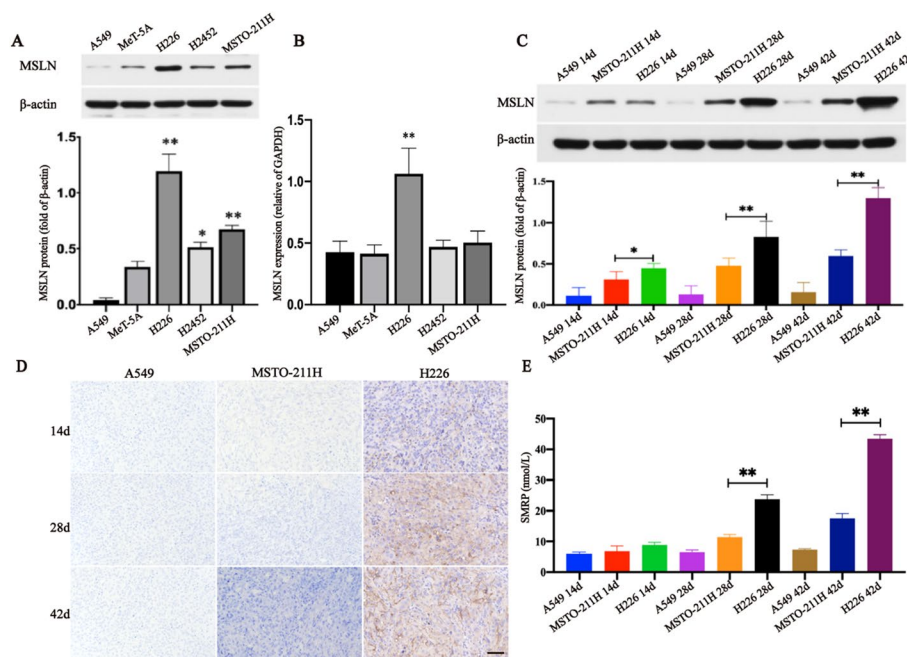

Fig. 1 Differential expression of MSLN in MPM subtypes. **A** Western blot and quantitative expression of MSLN in different MPM cells (H226, H2452, and MSTO-211H), MeT-5A, and A549 cells relative to β-actin. *$p < 0.05$, **$p < 0.01$, vs. MeT-5A. **B** mRNA expression of MSLN in the same cell lines as described in B, with GAPDH being the internal control. **$p < 0.01$, vs. other cells. **C** Western blot and quantification of MSLN in tumor tissues of tumor-bearing nude mice at 14, 28, and 42 days after molding, with β-actin being the loading control. **D** IHC staining for MSLN in tumor tissues of A549, MSTO-211H, and H226 cell lines, scale bar: 50 μm. **E** ELISA for SMRP in tumor-bearing mouse serum. Data are represented by means ± SEM. One-way ANOVA with Tukey's multiple comparisons test (**A**, **B**, **C**, **E**). *$p < 0.05$; **$p < 0.01$

H226 cells in tumor-bearing nude mice (Fig. 1E). As MeT-5A and H2452 cells failed to grow into tumors in the axils of nude mice, subsequent in vivo experiments did not involve MeT-5A and H2452 cells.

MSLN enhanced migration and invasion

To investigate the relationship between MSLN expression and MPM invasion and migration, we first determined the differences in cell migration and invasion among MPM cells, as these behaviors are the most prominent hallmarks of malignant cells. Compared with the migration rate between different cells at various time points (36–0 h), the migration rates of the different histological MPM cell types (H2452, MSTO-211H, and H226) were higher than those of MeT-5A cells; the highest mobility was found in MSTO-211H cells, as observed in the wound-scratch assay (Fig. 2A and B). We also examined the role of the histological subtypes in MPM cell movement and invasion by performing a Boyden chamber assay. In contrast to the MeT-5A and H226 groups, the MSTO-211H and H2452 groups showed higher numbers of migratory cells and higher absorbance (higher OD values). In addition, the number of migrated cells and the OD value of H226 cells were greater than those of MeT-5A cells (Fig. 2C and D). We conducted these experiments using a Transwell chamber with Matrigel. MPM cells showed higher invasive ability and OD values than MeT-5A cells. The invasive ability of MSTO-211H cells was significantly higher than that of H2452 and H226 cells. However, the differences in invasion and OD values between H2452 and H226 cells were not statistically significant (Fig. 2E and F). Overall, biphasic MSTO-211H cells were more invasive and migratory than epithelial H226 cells. We also found that the tumor growth rate of MSTO-211H cells was significantly higher than that of H226 cells, and that the survival period of the MSTO-211H group was shorter (Fig. 2G and H).

To investigate the MSLN migration and invasion regulation mechanisms, we first detected MSLN protein levels and mRNA expression in H226 cells after lentiviral transfection using western blotting and real-time quantitative RT-PCR assays. The results showed that the relative levels of MSLN protein and mRNA levels of MSLN were considerably higher in the LV-MSLN group than in the LV-NC or NC groups (Fig. 3A and B). We then studied classic molecules such as N-cadherin, MMP7, and MMP9, which act downstream of MSLN and regulate tumor cell migration and invasion, by western blotting. After MSLN protein overexpression in H226 cells, the expression levels of N-cadherin, MMP7, and MMP9 increased in the LV-MSLN group, and the increases in MMP7 and MMP9 were more prominent (Fig. 3C–F). The scratch assay migration rate (Fig. 4A and B), number of transwell-migrated cells (Fig. 4C), number of transwell-invaded cells (Fig. 4E), and corresponding crystal violet staining OD values (Fig. 4D and F) were significantly higher, and the survival period of nude mice was shorter (Fig. 4G). These results indicate that MSLN in H226 cells promotes the migratory and invasive abilities of tumors by regulating N-cadherin, MMP7, and MMP9.

FSPM preparation and characterization

The steps for synthesizing FSPM are illustrated in Additional file 1: Fig. S1. Successful modification with the anti-MSLN antibody was verified by XPS. The FSPM spectrum (Fig. 5B) showed a considerable drop in C–O bonding and an increase in C=O
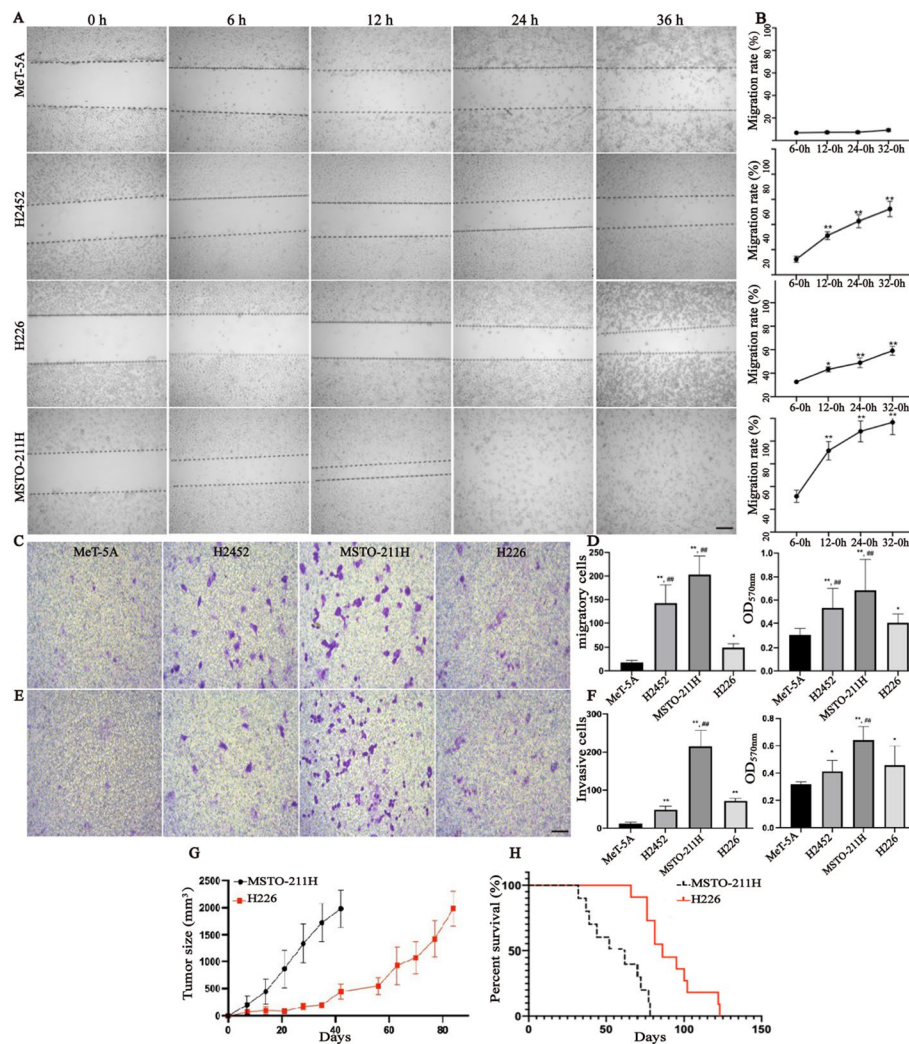
Fig. 2 The histological subtype of MPM is closely associated with cell migration, invasion, and survival. **A** Cell migration analysis of MeT-5A and MPM cells (H2452, H226, and MSTO-211H) at 0 h, 6 h, 12 h, 24 h, and 36 h in the scratch assay. **B** Migration rate line graph at 6-0 h, 12-0 h, 24-0 h, and 36-0 h. *$p < 0.05$, **$p < 0.01$, *vs.* 6–0 h. **C-D** Representative images (**C**) and quantitative analysis (**D**, migratory cells and crystal violet assays with OD values at 570 nm [OD_{570nm}]) of MPM cell and MeT5A cell migration were detected by Transwell migration assay. **E**, **F** Representative images (**E**) and quantitative analysis (**F**, invasive cells and crystal violet staining with OD570nm) of MPM cells and MeT5A invasion from Matrigel-coated Transwell. *$p < 0.05$, **$p < 0.01$, vs. MeT-5A; #$p < 0.05$, ##$p < 0.01$, vs. H226. **G**, **H** Tumor growth curves (**G**) and survival curves (**H**) in MSTO-211H and H226 tumor-bearing nude mice. Scale bar: 50 μm. One-way ANOVA with Tukey's multiple comparisons test (**B**, **D**, **F**)

bonding as compared to that observed in the FSP spectrum (Fig. 5A), which indicated more amide reactions occur between the COOH of FSP and the NH2 of the MSLN antibody, thus indirectly reacting to the success of antibody encapsulation. The morphology of the nanoparticles was characterized using TEM. The TEM images showed that the sample was uniform and spherical, and the size of the particles was approximately 120 nm (Fig. 5C). An MRI analyzer was used to detect the T_2 and T_1 relaxation times of the nanoprobes at different concentrations of Fe^{3+}. The plotted standard curve (Fig. 5D) showed that the transverse relaxation rate of the nanoprobe R_2 was 62.33 mM/s and the longitudinal relaxation rate R_1 was 0.08317 mM/s.
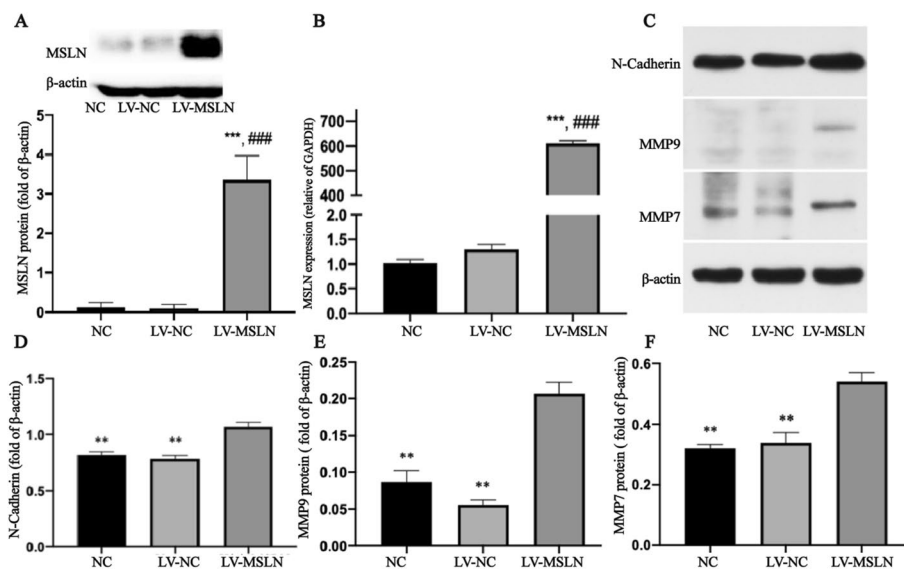
Fig. 3 Upregulation of MSLN promotes the expression of N-Cadherin, MMP7, and MMP9. **A** Western blot assay and relative expression of MSLN among NC, empty vector control (LV-NC), and MSLN overexpression (LV-MSLN) groups. **B** MSLN mRNA expression in NC, LV-NC, and LV-MSLN cells. ***$p < 0.05$, vs. NC; ###$p < 0.01$, vs. LV-NC. **C** Protein levels of N-Cadherin, MMP9, and MMP7 in H226 cells were markedly enhanced in the LV-MSLN group. **D** Quantitative analysis of N-Cadherin, **E** quantitative analysis of MMP9, **F** quantitative analysis of MMP7. GAPDH and β-actin served as internal controls in these assays. **$p < 0.01$, vs. LV-MSLN. One-way ANOVA with Tukey's multiple comparisons test (**A**, **B**, **D**, **E**, **F**)

This indicates that the nanoprobe is a good negative contrast agent that significantly decreases the T2 signal.

The cellular uptake was evaluated in vitro to assess FSPM targeting. Prussian staining was performed to evaluate the target-binding potential of the FSPM nanoprobes in A549 and H226 cells (Fig. 5E). Many blue particles were detected when FSPM was seeded into the H226 cell solution, indicating that FSPM was taken up by H226 cells, almost rare blue particles were detected in A549 cells treated with either FSP or FSPM, which was also confirmed in the quantitative analysis of Prussian cell (Fig. 5F). These data demonstrate that the anti-MSLN antibody-modified FSPM probe could identify MSLN-expressing H226 cells. Next, we evaluated the in vitro cytotoxicity of FSPM using the CCK8 assay (Fig. 5H). The viability of the A549 and H226 cell lines was > 90%, even after incubation with NPs at high concentrations (200 µg/mL), indicating that the polymer material was nontoxic.

The excised tumors and main organs were examined using ICP and hematoxylin and eosin (H&E) staining to evaluate the concentration of Fe^{3+} and toxicity in vivo. The tumors in the FSPM group had much higher Fe^{3+} concentrations than those in the FS group. When compared with the FSPM group, the FS group had a higher liver Fe^{3+} concentration. The differences in Fe^{3+} concentrations in other organs were not significant (Fig. 5G). Representative H&E-stained images are shown in Fig. 5I. Obvious pathological changes such as necrosis, fibrosis and injury were not observed in these organs. We also evaluated the stability of the FSPM. We did not observe agglomeration of the nanoprobes, even after incubation for 24 h in PBS or saline, confirming the
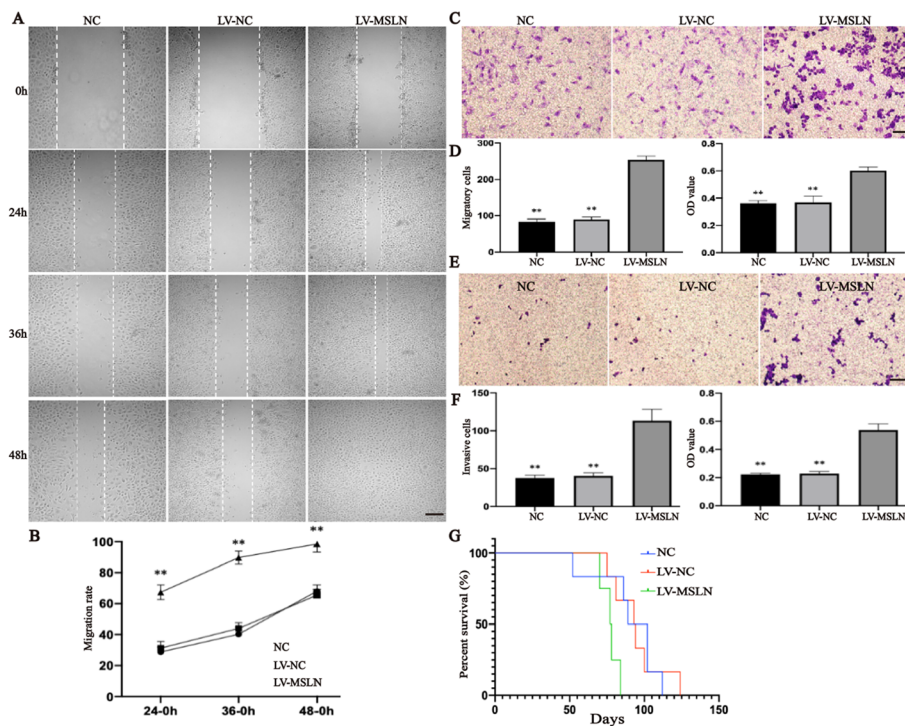
Fig. 4 Overexpression of MSLN promotes cell migration and invasion. Wound healing assay (**A**) and quantification of migration rate at different time points (**B**) in NC, LV-NC, and LV-MSLN cells. **p < 0.01, vs. NC. **C** Representative images of Transwell migration assay and the number of migrating cells as well as OD Values (**D**). **E** Transwell invasion assay and quantitative analysis of invasive cells together with OD values (**F**). **p < 0.01, vs. LV-MSLN. **G**: Survival curves of tumor-bearing nude mice with NC, LV-NC, and LV-MSLN cells. Scale bar: 50 μm. One-way ANOVA with Tukey's multiple comparisons test (**B**, **D**, **F**)

stability of FSPM (Additional file 1: Fig. S2). These findings indicate that the FSPM nanomaterials are suitable for MRI applications.

Targeted imaging of FSPM in vitro and in vivo detected MSLN status

To assess the targeted imaging of the FSPM, in vitro targeted MRI was performed. Owing to its high transverse relaxation rate and good cell compatibility, the FSPM serves as a negative contrast agent for MR T2WI and T2 mapping imaging in vitro. After incubating the cells (A549, MeT-5A, H226, H2452, and MSTO-211H) with FSPM at different concentrations of Fe^{3+}, the A549 and MeT-5A groups showed slight uptake of FSPM, but did not show changes in T2 signal intensity and T2 values with increasing Fe^{3+} concentration. However, the T2 signal intensity and T2 values were lower at Fe^{3+} concentrations of 40 and 60 μg/mL than at 0 μg/mL in the H2452 and MSTO-211H groups (Fig. 6A–C). In addition, the cells in the H226 group showed a lower T2 signal intensity and T2 value after binding to nanoprobes with different concentrations of Fe^{3+}. When the concentration of Fe^{3+} was 60 μg/mL, the T2 signal intensity and T2 values were lower in the H226 group than in the MSTO-211H, H2452, MeT-5A, and A549 groups. This result was consistent with MSLN cell expression; when MSLN expression was higher, more FSPM was bound to it, further decreasing T2 signal intensity.
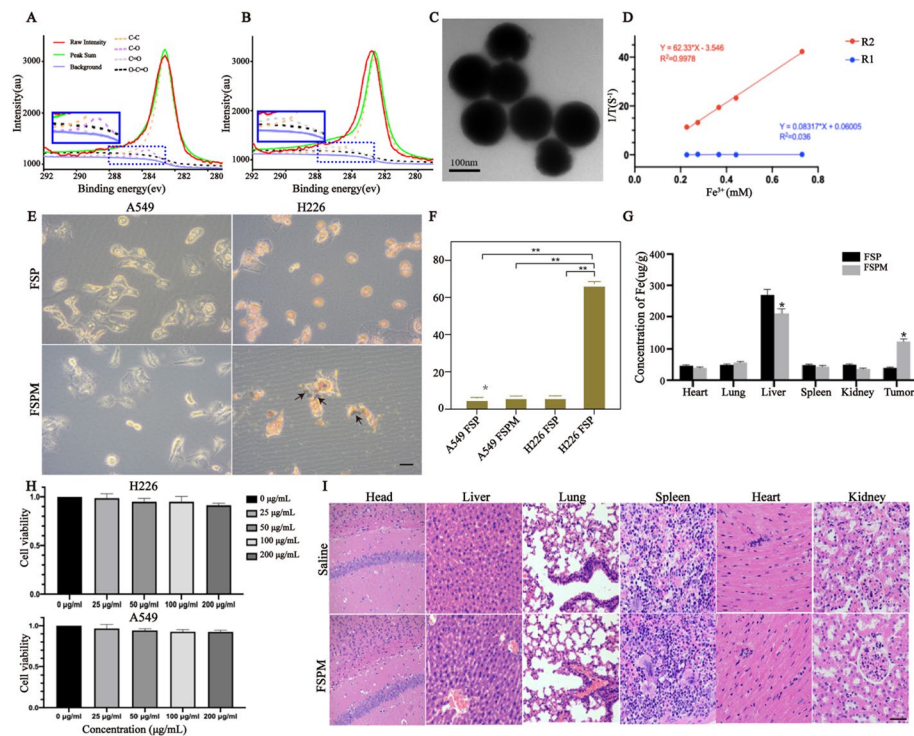
Fig. 5 Characterization and properties of the FSPM. XPS spectra of FSP (**A**) and (**B**) FSPM. **C** TEM images of the FSPM. **D** T2 relaxation rate (R2) and T1 relaxation rate (R1) of FSPM as a function of iron concentration. **E** Prussian blue staining showed iron-containing cells (black arrow), scale bar: 20 μm. **F** Quantitative analysis of Prussian-stained cell areas. SD: Standard deviation (*$p < 0.05$; **$p < 0.01$). **G** Fe^{3+} distribution in heart, lung, liver, spleen, kidney, and tumor tissues after injection of FSP and FSPM. *$p < 0.05$, vs. FSP. **H** Cell viability of A549 and H226 cells after incubation with FSPM at different concentrations. **I** Sections of the head, liver, lung, spleen, heart, and kidney, after injection of saline and FSPM (H&E stain 10 × magnification, scale bars: 50 μm). Abbreviation: FSP, $Fe_3O_4@SiO_2$-PEG; FSPM, $Fe_3O_4@SiO_2$-PEG-MSLN. One-way ANOVA with Tukey's multiple comparisons test (**F**, **G**, **I**)

Next, we conducted in vivo MRI of the FSPM. We found that the T2 signal intensity and T2 values of the tumor tissues in the A549, MSTO-211H, and H226 groups were not significantly different at each time point when saline and FSP were injected. When FSPM were injected 42 days after tumor formation, the T2 signal intensity and T2 values decreased slightly after injection in the A549 and MSTO-211H groups, before recovering. However, T2 signal intensity and T2 values of tumor tissues in the H226 group continued to decrease over time after the injection of FSPM, and at 3.5 h the relative T2 signal intensity and T2 values were the lowest in the H226 group. (Fig. 7A–F). Around 14 days after molding, the relative T2 signal intensity of H226 group decreased significantly at 1.5 and 2.5 h, and the T2 values dropped within 1.5–3.5 h after FSPM injection (Additional file 1: Fig. S3). After 28 days molding, the T2 signal decreased in the MSTO-211H group 1.5 h after FSPM was injected, and the T2 values decreased 2.5 h and 3.5 h, but in the H226 group, the T2 signal intensity also decreased at 1.5 h, and the T2 values decreased within 1.5–3.5 h (Additional file 1: Fig. S4). Moreover, when compared with the MSTO-211H group, the T2 signal intensity and T2 value decreased more in the H226 group at all time points after FSPM injection, and no significant difference was observed after the A549 group was
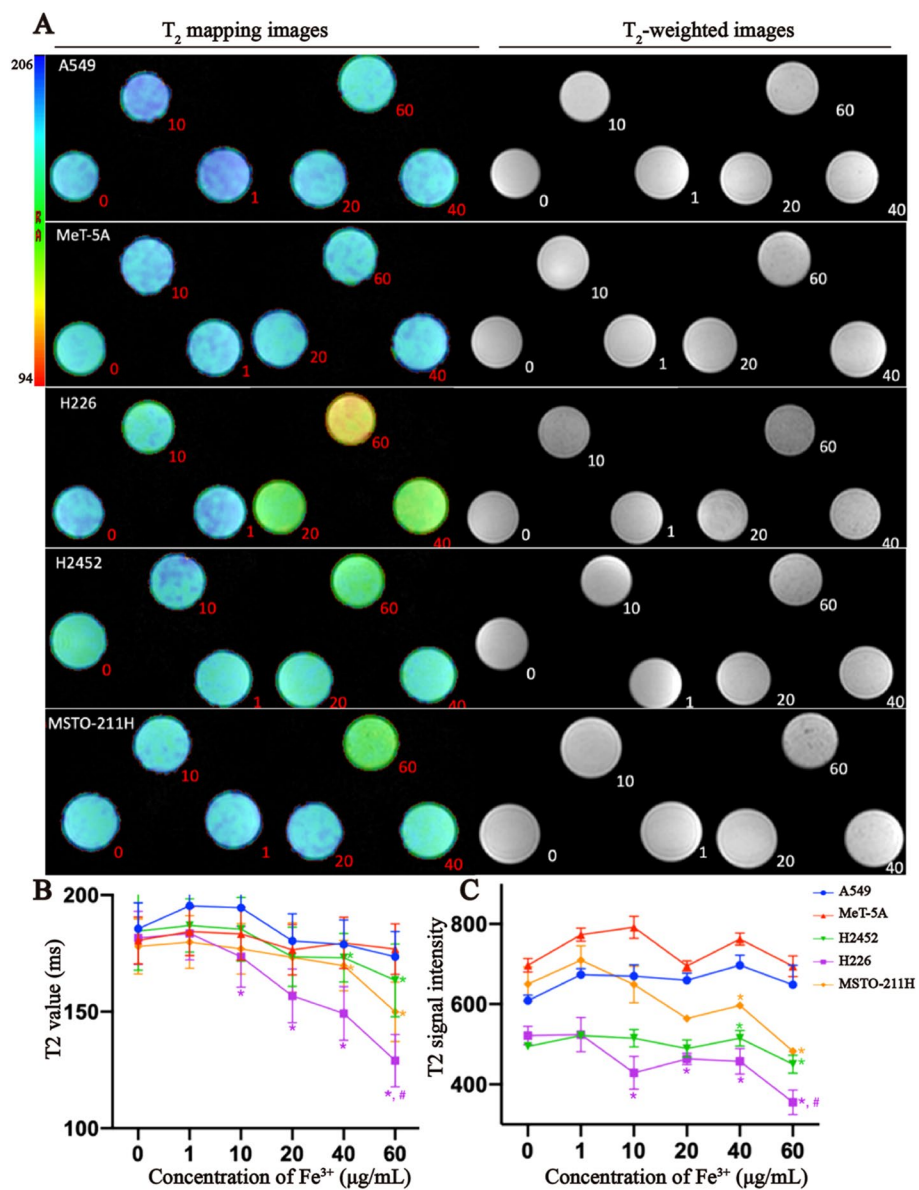
Fig. 6 Targeted MRI examination of FSPM in vitro. **A** T2WI and T2 mapping MRI examinations of FSPMs with different iron ion concentrations (0, 1, 10, 20, 40, and 60 µg/mL) after incubation with A549, MeT-5A, and MPM cells. **B**, **C** T2 value and T2 signal intensity changes under the Fe^{3+} gradient concentration. FSP, Fe_3O_4@SiO_2-PEG; FSPM, Fe_3O_4@SiO_2-PEG-MSLN. *$p < 0.05$, vs. 0 µg/mL; # $p < 0.05$ vs. other groups. One-way ANOVA with Tukey's multiple comparisons test (**B**, **C**)

injected with FSPM at different time points. These results corresponded to the quantity of MSLN protein present in MPM cells.

Discussion

Herein, MSLN was found to be highly expressed in MPM cells. The levels of MSLN expression and the invasive and migratory abilities were different in different histological subtypes of MPM cells. Overexpression of MSLN enhances MPM tumor cell migration and invasion through the regulation of N-cadherin, MMP7, and MMP9, which in turn
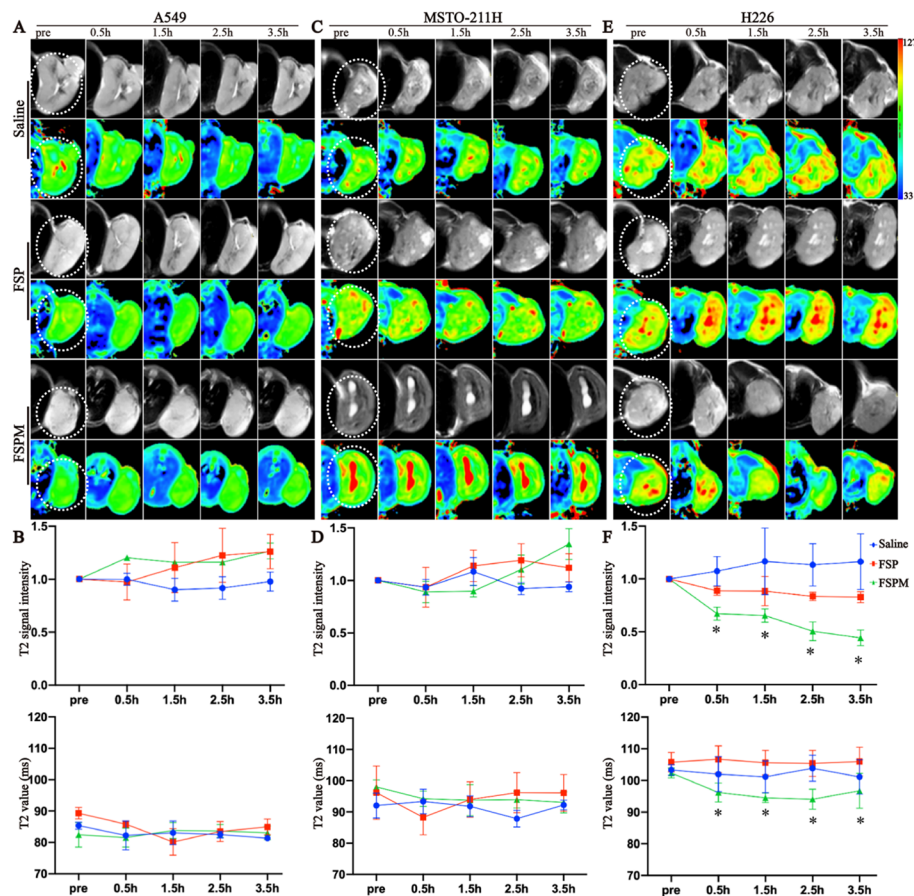
Fig. 7 Targeted MRI examination of FSPM in vivo. **A**, **C**, and **E** 42 days after tumor transplantation. In vivo T2WI and T2 mapping of nude mice at different time points (0, 0.5, 1.5, 2.5, and 3.5 h) after injection of saline, FSP, and FSPM in A549, MSTO-211H, and H226 groups. **B**, **D**, and **F** Corresponding T2 signal intensity and T2 value changes in tumor tissues (lower). *$p < 0.05$, vs. before injection. One-way ANOVA with Tukey's multiple comparisons test (**B**, **D**, **F**), $n = 3$

reduces the survival of tumor-bearing mice. We constructed an MSLN-targeted MRI nanoprobe to recognize and differentiate histological subtypes of MPM based on MSLN levels. Our findings indicate that MRI nanoprobes could potentially contribute to the noninvasive assessment of MSLN status, aid in diagnosis, distinguish histological subtypes, and evaluate migration, invasion, and prognosis of MPM.

MSLN expression levels were evaluated, and the relationship between MSLN expression, migration, and invasion in MPM was confirmed. We detected MSLN expression in various cell lines and mouse models at different time points using western blotting, RT-PCR, IHC, and ELISA. While cross-comparison of diverse experimental results may be challenging, they all demonstrate MSLN expression was greater in the H226 (epithelial type), and increased continuously with the progression of tumor growth. These results were similar to those of previous study (Melaiu et al. 2014). However, the histological types of MPM and MSLN expression do not exhibit absolute correlation. In this study, it was observed that the MSLN expression in H2452 (epithelioid type) did not surpass that of MSTO-211H (biphasic type), which is consistent with literature reports (Kojima et al. 2020a, b).

In addition, the migratory and invasive abilities differed MPM histological subtypes; migration and invasion of biphasic cells (MSTO-211H) were higher, and these cells showed a faster increase in the tumor volume but shorter survival. Some investigations have revealed that high MSLN expression is linked to greater invasiveness, migration, and proliferation (Servais et al. 2012; Kachala et al. 2014); however, the exact regulatory mechanisms remain unclear. Interestingly, in our study, epithelial MPM showed higher MSLN expression than biphasic MPM, but the invasive and migratory abilities of epithelial MPM were lower than those of biphasic MPM. MPM is often divided into three histological subtypes: epithelioid, biphasic, and sarcomatoid, and with median survival times of 15–19, 10–12, and 4–10 months, respectively (Yap et al. 2017; Milano and Zhang 2010). This shows that the "pathological histological subtype" is an indispensable factor in determining the prognosis of MPM. However, the expression of MSLN does not directly affect the histological differentiation of MPM (Kojima et al. 2020a, b; Verma et al. 2018). Moreover, considering MPM with the same pathological histological subtype, higher MSLN expression indicates tumor progression or recurrence (de Fonseka et al. 2018).Meanwhile, after surgical resection of MPM, patients with lower MSLN expression survive longer (Hanaoka et al. 2017). Additionally, we found that MSLN-overexpression in H226 cells enhanced tumor migration and invasion by regulating key molecules such as N-Cadherin, MMP7, and MMP9. These molecules, widely recognized for promoting tumor migration and invasion in lung, liver, ovarian, breast, and kidney cancers (Labernadie et al. 2017; Yang et al. 2017). Of course, further analysis of the expression levels of MMP-9, MMP-7 and N-cadherin in H2452 and MSTO-211H, compared with the expression levels of NC, LV-NC and LV-MSLN, may lead to a deeper understanding of their roles in different cancer subtypes related to MSLN levels and migration/invasion characteristics. In summary, our results showed that MSLN expression may be strongly associated with prognosis, and the intrinsic influences on mesothelioma differentiation need to be further investigated.

After confirming the role of MSLN and the mechanisms through which it regulates migration and invasion in MPM, we constructed a targeted MPM probe, FSPM, coated with an MSLN antibody. Our probe had a regular morphology, a suitable particle size (120 nm), good water dispersibility, and was nontoxic. It also decreased the T2 value, indicating that it is an effective contrast agent for MPM. Prussian blue staining experiments showed that FSPM could specifically recognize cells that expressed MSLN, and the ICP assay of Fe^{3+} concentration further confirmed the targeting of FSPM to MPM cells. Additionally, in vitro MRI imaging of FSPM showed that as the concentration of Fe^{3+} increased, the T2 signal intensity and T2 value of H226 cells decreased significantly. When the Fe^{3+} concentration was 60 μg/mL, the T2 signal intensity and T2 value of H226 cells were lower than those of other cells (given the high expression of MSLN in H226 cells), which indicated that the MSLN-targeting nanoprobe was not only targeted but also related to the level of expression of MSLN in tumor cells. These results were similar to those of a study in which a nanoprobe targeting the αvβ3 receptor was investigated (Zhang et al. 2018).

A systematic in vivo evaluation indicated that FSPM had excellent MRI properties and could target human MPM xenografts in nude mice. Changes in T2 signal intensity and T2 values in tumor tissues were similar to those observed in tumor cells. We found that,

after the injection of FSPM, the T2 signal intensity and T2 value of tumor tissues in the H226 group continued to decrease over time (0, 0.5, 1.5, 2.5, and 3.5 h), and the T2 signal intensity and T2 value decreased more in the H226 group than in the MSTO-211H group at 14, 28, and 42 days after molding. Interestingly. Figure 6C suggests a decrease in T2 signal intensity in MSTO-211H, similar to H226 with Fe^{3+} concentration increase, despite MSTO-211H lacking MSLN expression. However, T2 mapping shows a more significant difference in T2 values between H226 concentrations than MSTO-211H. This variation may be due to the influence of field uniformity and noise on T2 signal intensity, causing differences in T2 signals among cell lines. Therefore, it is suggested to use more stable and reliable T2 values under T2 mapping as a more objective quantitative parameter. Ultimately, all experimental results indicate that FSPM might be a good T2 negative contrast agent for MRI in MPM, and the T2 signal intensity and T2 values might indirectly reflect the expression level of the MSLN. This indicated that the higher the MSLN expression, the lower the T2 signal intensity and T2 value. Therefore, FSPM might be used to evaluate the MSLN status, and based on the biological information obtained from MSLN, FSPM can be further used to detect, and differentiate histological subtypes, access the migration/invasive capacity, and predict MPM prognosis.

Our study has several limitations. First, we were unable to investigate sarcomatoid MPM cells or tumor tissue samples from patients with MPM. The rarity of MPM poses challenges in collecting samples, thereby limiting the scope of our study. Second, although we made a lot of efforts and attempts, we failed to successfully constructed a stable MSLN-down-regulated H226 cell line. This limitation should be addressed in future studies by reconstituting experiments using a broader range of MPM cell lines. Finally, while our study demonstrates the potential of nanoprobes for monitoring MSLN expression, more extensive research is needed to establish the correlation between MSLN expression levels and imaging signals obtained in MPM patients. Moreover, future work will employ IgG-modified probes as specificity controls for anti-MSLN-FSPM investigations. Through TEM and spectroscopy, we will monitor nanoparticle core-shell morphology and functionality over time, enriching insights into nanoparticle behavior and dynamics.

Conclusions

MPM tumor cells specifically expressed MSLN at varying levels across histological subtypes and growth stages. MSLN facilitates tumor cell migration and invasion by regulating N-cadherin, MMP7, and MMP9. Building upon this understanding, we developed an MRI nanoprobe that targets MSLN to assess its status. This nanoprobe may be helpful for early detection, identification of histological subtypes, evaluation of migration/invasion potential, and prognosis assessment for MPM.

Abbreviations

CT	Computer tomography
cDNA	Complementary DNA
CA125	Carbohydrate antigen 125
CCK-8	Cell Counting Kit-8
DI	Deionized
ELISA	Enzyme-linked immunosorbent assay
FDG	Fluorodeoxyglucose
FDA	Food and Drug

FBS	Fetal bovine serum
FSP	$Fe_3O_4@SiO_2$-PEG
FSPM	$Fe_3O_4@SiO_2$-PEG-MSLN
GAPDH	Glyceraldehyde-3-phosphate dehydrogenase
HER2	Human epidermal growth factor receptor 2
HER1	Human epidermal growth factor receptor 1
HRP	Horseradish peroxidase
H&E	Hematoxylin and eosin
IHC	Immunohistochemistry
ICP	Inductively coupled plasma
LV-MSLN	MSLN-overexpressing group
LV-NC	Lentiviral vector
MSLN	Mesothelin
MPM	Malignant pleural mesothelioma
MRI	Magnetic resonance imaging
MMP-7	Matrix metallopeptidase 7
MUC16	Mucin 16
NC	Negative control
NP	Nanoparticle
OD	Optical density
PET	Positron emission tomography
PBS	Phosphate-buffered saline
PEG	Polyethylene glycol
RT-PCR	Reverse transcription-polymerase chain reaction
SMRP	Soluble mesothelin-related peptide
SPECT	Single-photon emission computed tomography
SPIONs	Superparamagnetic iron oxide nanoparticles
SDS	Sodium dodecyl sulfate
T2WI	T2-weighted imaging
TBST	Tris-buffered saline twee
TEM	Transmission electron microscope
XPS	X-ray photoelectron spectroscopy
$FeCl_3 \cdot 6H_2O$	Ferric chloride hexahydrate
Fe^{3+}	Iron ions

Supplementary Information

The online version contains supplementary material available at https://doi.org/10.1186/s12645-023-00238-y.

> **Additional file 1: Table S1.** The primer sequences of *GAPDH* and *MSLN*. **Table S2.** The MRI scan parameters. **Fig. S1** Schematic diagram of FSPM nanoprobe to MPM cells, together with the T2W and T2 mapping images in vivo. **Fig. S2** Stability of FSPM solution in saline and FBS at different concentrations. **Fig. S3** Targeted MRI examination of FSPM in vivo (14 d after tumor transplantation). **Fig. S4** Targeted MRI examination of FSPM in vivo (28 d after tumor transplantation).

Author contributions
DH conceived and designed this study; YH conducted the most of experiments; JX assisted with immunohistochemistry experiments and related data interpretation; BC, XH, and CL were responsible for molecularly targeted nanoprobe preparation and the performance evaluation of the probes. JM, TQ, CG, and BH helped complete a related study of animal MRI imaging. GL and FL contributed to the experimental techniques of immunoblotting, PCR, and Lentivirus infection. SS and YH were engaged in manuscript writing. All authors have read and endorsed the final manuscript.

Availability of data and materials
This article contains all of the study's raw data and analytical results (along with the associated Supplementary Information files).

Declarations

Ethics approval and consent to participate
Permission for all animal research was received from the Animal Care and Use Committee of Kunming Medical University (No. KMMU2021741).

Consent for publication
All authors read and approved the final version of the manuscript.

Competing interests
The authors declare no conflict of interest between them.

References

An Z, Dobra K, Lock JG, Strömblad S, Hjerpe A, Zhang H (2010) Kindlin-2 is expressed in malignant mesothelioma and is required for tumor cell adhesion and migration. Int J Cancer 127:1999–2008

Bulte JWM (2019) Superparamagnetic iron oxides as MPI tracers: a primer and review of early applications. Adv Drug Deliv Rev 138:293–301

Chang MC, Chen CA, Chen PJ, Chiang YC, Chen YL, Mao TL, Lin HW, Lin Chiang WH, Cheng WF (2012) Mesothelin enhances invasion of ovarian cancer by inducing MMP-7 through MAPK/ERK and JNK pathways. Biochem J 442:293–302

Chen SH, Hung WC, Wang P, Paul C, Konstantopoulos K (2013) Mesothelin binding to CA125/MUC16 promotes pancreatic cancer cell motility and invasion via MMP-7 activation. Sci Rep 3:1870

Craighead JE, Mossman BT (1982) The pathogenesis of asbestos-associated diseases. N Engl J Med 306:1446–1455

Cristaudo A, Bonotti A, Simonini S, Vivaldi A, Guglielmi G, Ambrosino N, Chella A, Lucchi M, Mussi A, Foddis R (2011) Combined serum mesothelin and plasma osteopontin measurements in malignant pleural mesothelioma. J Thorac Oncol 6:1587–1593

de Fonseka D, Arnold DT, Stadon L, Morley A, Keenan E, Darby M, Armstrong L, Virgo P, Maskell NA (2018) A prospective study to investigate the role of serial serum mesothelin in monitoring mesothelioma. BMC Cancer 18:199

Gao P, Mei C, He L, Xiao Z, Chan L, Zhang D, Shi C, Chen T, Luo L (2018) Designing multifunctional cancer-targeted nanosystem for magnetic resonance molecular imaging-guided theranostics of lung cancer. Drug Deliv 25:1811–1825

Ghosh SK, Uchida M, Yoo B, Ross AW, Gendler SJ, Gong J, Moore A, Medarova Z (2013) Targeted imaging of breast tumor progression and therapeutic response in a human uMUC-1 expressing transgenic mouse model. Int J Cancer 132:1860–1867

Hanaoka T, Hasegawa K, Kato T, Sato S, Kurosaki A, Miyara A, Nagao S, Seki H, Yasuda M, Fujiwara K (2017) Correlation between tumor mesothelin expression and serum mesothelin in patients with epithelial ovarian carcinoma: a potential noninvasive biomarker for mesothelin-targeted therapy. Mol Diagn Ther 21:187–198

Hao B, Wei L, Cheng Y, Ma Z, Wang J (2022) Advanced nanomaterial for prostate cancer theranostics. Front Bioeng Biotechnol 10:1046234

Hollevoet K, Reitsma JB, Creaney J, Grigoriu BD, Robinson BW, Scherpereel A, Cristaudo A, Pass HI, Nackaerts K, Rodríguez Portal JA, Schneider J, Muley T, Di Serio F, Baas P, Tomasetti M, Rai AJ, van Meerbeeck JP (2012) Serum mesothelin for diagnosing malignant pleural mesothelioma: an individual patient data meta-analysis. J Clin Oncol 30:1541–1549

Jarockyte G, Daugelaite E, Stasys M, Statkute U, Poderys V, Tseng TC, Hsu SH, Karabanovas V, Rotomskis R (2016) Accumulation and toxicity of superparamagnetic iron oxide nanoparticles in cells and experimental animals. Int J Mol Sci 17:1193

Kachala SS, Bograd AJ, Villena-Vargas J, Suzuki K, Servais EL, Kadota K, Chou J, Sima CS, Vertes E, Rusch VW, Travis WD, Sadelain M, Adusumilli PS (2014) Mesothelin overexpression is a marker of tumor aggressiveness and is associated with reduced recurrence-free and overall survival in early-stage lung adenocarcinoma. Clin Cancer Res 20:1020–1028

Katz SI, Roshkovan L, Berger I, Friedberg JS, Alley EW, Simone CB 2nd, Haas AR, Cengel KA, Sterman DH, Albelda SM (2021) Serum soluble mesothelin-related protein (SMRP) and fibulin-3 levels correlate with baseline malignant pleural mesothelioma (MPM) tumor volumes but are not useful as biomarkers of response in an immunotherapy trial. Lung Cancer 154:5–12

Kobayashi K, Sasaki T, Takenaka F, Yakushiji H, Fujii Y, Kishi Y, Kita S, Shen L, Kumon H, Matsuura E (2015) A novel PET imaging using ^{64}Cu-labeled monoclonal antibody against mesothelin commonly expressed on cancer cells. J Immunol Res 2015:268172

Kojima M, Kajino K, Momose S, Wali N, Hlaing MT, Han B, Yue L, Abe M, Fujii T, Ikeda K, Hino O (2020a) Possible reversibility between epithelioid and sarcomatoid types of mesothelioma is independent of ERC/mesothelin expression. Respir Res 21:187

Labernadie A, Kato T, Brugués A, Serra-Picamal X, Derzsi S, Arwert E, Weston A, González-Tarragó V, Elosegui-Artola A, Albertazzi L, Alcaraz J, Roca-Cusachs P, Sahai E, Trepat X (2017) A mechanically active heterotypic E-cadherin/N-cadherin adhesion enables fibroblasts to drive cancer cell invasion. Nat Cell Biol 19:224–237

Li X, Wang R, Zhang Y, Han S, Gan Y, Liang Q, Ma X, Rong P, Wang W, Li W (2022) Molecular imaging of tumor-associated macrophages in cancer immunotherapy. Ther Adv Med Oncol 14:17588359221076194

Liu F, Le W, Mei T, Wang T, Chen L, Lei Y, Cui S, Chen B, Cui Z, Shao C (2016) In vitro and in vivo targeting imaging of pancreatic cancer using a Fe3O4@SiO2 nanoprobe modified with anti-mesothelin antibody. Int J Nanomed 11:2195–2207

Liu B, van Gerwen M, Bonassi S, Taioli E, International Association for the Study of Lung Cancer Mesothelioma Task F (2017) Epidemiology of environmental exposure and malignant mesothelioma. J Thorac Oncol 12:1031–1045

Lo Russo G, Tessari A, Capece M, Galli G, de Braud F, Garassino MC, Palmieri D (2018) MicroRNAs for the diagnosis and management of malignant pleural mesothelioma: a literature review. Front Oncol 8:650

Luo S, Liu X, Mu S, Tsai SP, Wen CP (2003) Asbestos related diseases from environmental exposure to crocidolite in Da-yao, China. I. Review of exposure and epidemiological data. Occup Environ Med 60:35–41; discussion 41-2

Melaiu O, Stebbing J, Lombardo Y, Bracci E, Uehara N, Bonotti A, Cristaudo A, Foddis R, Mutti L, Barale R, Gemignani F, Giamas G, Landi S (2014) MSLN gene silencing has an anti-malignant effect on cell lines overexpressing mesothelin deriving from malignant pleural mesothelioma. PLoS ONE 9:e85935

Mensi C, Riboldi L, De Matteis S, Bertazzi PA, Consonni D (2015) Impact of an asbestos cement factory on mesothelioma incidence: global assessment of effects of occupational, familial, and environmental exposure. Environ Int 74:191–199

Milano MT, Zhang H (2010) Malignant pleural mesothelioma: a population-based study of survival. J Thorac Oncol 5:1841–1848

Montemagno C, Bacot S, Ahmadi M, Kerfelec B, Baty D, Debiossat M, Soubies A, Perret P, Riou L, Fagret D (2018) Preclinical evaluation of mesothelin-specific ligands for SPECT imaging of triple-negative breast cancer. J Nucl Med 59:1056–1062

Nickell LT Jr, Lichtenberger JP 3rd, Khorashadi L, Abbott GF, Carter BW (2014) Multimodality imaging for characterization, classification, and staging of malignant pleural mesothelioma. Radiographics 34:1692–1706

Pastan I, Hassan R (2014) Discovery of mesothelin and exploiting it as a target for immunotherapy. Cancer Res 74:2907–2912

Prantner AM, Yin C, Kamat K, Sharma K, Lowenthal AC, Madrid PB, Scholler N (2018) Molecular imaging of mesothelin-expressing ovarian cancer with a human and mouse cross-reactive nanobody. Mol Pharm 15:1403–1411

Rowe SP, Pomper MG (2022) Molecular imaging in oncology current impact and future directions. CA Cancer J Clin 72:333–352

Servais EL, Colovos C, Rodriguez L, Bograd AJ, Nitadori J, Sima C, Rusch VW, Sadelain M, Adusumilli PS (2012) Mesothelin overexpression promotes mesothelioma cell invasion and MMP-9 secretion in an orthotopic mouse model and in epithelioid pleural mesothelioma patients. Clin Cancer Res 18:2478–2489

Shen K, Liu K, Wang Y, Ni P, Xiao J, Hao F, Zhou X, Xu Z, Yang L (2022) Polymorphisms of an oncogenic gene, mesothelin, predict the risk and prognosis of gastric cancer in a Chinese Han population. Arch Toxicol 96:2097–2111

Shimizu A, Hirono S, Tani M, Kawai M, Okada K, Miyazawa M, Kitahata Y, Nakamura Y, Noda T, Yokoyama S, Yamaue H (2012) Coexpression of MUC16 and mesothelin is related to the invasion process in pancreatic ductal adenocarcinoma. Cancer Sci 103:739–746

Sinha S, Swift AJ, Kamil MA, Matthews S, Bull MJ, Fisher P, De Fonseka D, Saha S, Edwards JG, Johns CS (2020) The role of imaging in malignant pleural mesothelioma: an update after the 2018 BTS guidelines. Clin Radiol 75:423–432

Uribe Madrid SI, Pal U, Kang YS, Kim J, Kwon H, Kim J (2015) Fabrication of Fe3O4@mSiO2 core-shell composite nanoparticles for drug delivery applications. Nanoscale Res Lett 10:217

Verma V, Ahern CA, Berlind CG, Lindsay WD, Shabason J, Sharma S, Culligan MJ, Grover S, Friedberg JS, Simone CB 2nd (2018) Survival by histologic subtype of malignant pleural mesothelioma and the impact of surgical resection on overall survival. Clin Lung Cancer 19:e901–e912

Vigneswaran WT, Kircheva DY, Ananthanarayanan V, Watson S, Arif Q, Celauro AD, Kindler HL, Husain AN (2017) Amount of epithelioid differentiation is a predictor of survival in malignant pleural mesothelioma. Ann Thorac Surg 103:962–966

Wang P, Bai C, Shen S, Jiang C, Deng J, Han D (2021) MALAT1 promotes malignant pleural mesothelioma by sponging miR-141-3p. Open Med (wars) 16:1653–1667

Xie SQ, Zhang YH, Li Q, Xu FH, Miao JW, Zhao J, Wang CJ (2012) 3-Nitro-naphthalimide and nitrogen mustard conjugate NNM-25 induces hepatocellular carcinoma apoptosis via PARP-1/p53 pathway. Apoptosis 17:725–734

Xing H, Bu W, Zhang S, Zheng X, Li M, Chen F, He Q, Zhou L, Peng W, Hua Y, Shi J (2012) Multifunctional nanoprobes for upconversion fluorescence. MR and CT Trimodal Imaging Biomater 33:1079–1089

Yang S, Liu Y, Li MY, Ng CSH, Yang SL, Wang S, Zou C, Dong Y, Du J, Long X, Liu LZ, Wan IYP, Mok T, Underwood MJ, Chen GG (2017) FOXP3 promotes tumor growth and metastasis by activating Wnt/β-catenin signaling pathway and EMT in non-small cell lung cancer. Mol Cancer 16:124

Yap TA, Aerts JG, Popat S, Fennell DA (2017) Novel insights into mesothelioma biology and implications for therapy. Nat Rev Cancer 17:475–488

Zhang J, Bera TK, Liu W, Du X, Alewine C, Hassan R, Pastan I (2014) Megakaryocytic potentiating factor and mature mesothelin stimulate the growth of a lung cancer cell line in the peritoneal cavity of mice. PLoS ONE 9:e104388

Zhang Y, Zhu X, Liu L, Hong S, Zuo Z, Wang P, Su D (2018) Synthesis and in vitro study of a dual-mode probe targeting integrin αvβ3. Nanoscale Res Lett 13:281

Zhang Z, Shen S, Ma J, Qi T, Gao C, Hu X, Han D, Huang Y (2023) Sequential multi-parametric MRI in assessment of the histological subtype and features in the malignant pleural mesothelioma xenografts. Heliyon 9:e15237

Żuk M, Gawęda W, Majkowska-Pilip A, Osial M, Wolski M, Bilewicz A, Krysiński P (2021) Hybrid radiobioconjugated superparamagnetic iron oxide-based nanoparticles for multimodal cancer therapy. Pharmaceutics 13:1843

Publisher's Note